Iwao Nitta, Suvi Karvonen, Olli Himanen, and Mikko Mikkola, 2008, Modeling the effect of inhomogeneous compression of GDL on local transport phenomena in a PEM fuel cell, Espoo, Finland, 23 pages, Helsinki University of Technology Publications in Engineering Physics, TKK-F-A854, Fuel Cells, submitted for publication, 8th November 2007.

Helsinki University of Technology Publications in Engineering Physics
Teknillisen korkeakoulun teknillisen fysiikan julkaisuja
Espoo 2008 TKK-F-A854

MODELING THE EFFECT OF INHOMOGENEOUS COMPRESSION OF GDL ON LOCAL TRANSPORT PHENOMENA IN A PEM FUEL CELL

Iwao Nitta, Suvi Karvonen, Olli Himanen & Mikko Mikkola

TEKNILLINEN KORKEAKOULU
TEKNISKA HÖGSKOLAN
HELSINKI UNIVERSITY OF TECHNOLOGY
TECHNISCHE UNIVERSITÄT HELSINKI
UNIVERSITE DE TECHNOLOGIE D'HELSINKI

Helsinki University of Technology Publications in Engineering Physics
Teknillisen korkeakoulun teknillisen fysiikan julkaisuja
Espoo 2008 TKK-F-A854

MODELING THE EFFECT OF INHOMOGENEOUS COMPRESSION OF GDL ON LOCAL TRANSPORT PHENOMENA IN A PEM FUEL CELL

Iwao Nitta, Suvi Karvonen, Olli Himanen & Mikko Mikkola

Helsinki University of Technology
Faculty of Information and Natural Sciences
Department of Engineering Physics

Distribution:
Helsinki University of Technology
Advanced Energy Systems
P.O. Box 4100
02015 TKK
Finland
URL: http://www.tkk.fi/Units/AES/
Tel. +358-9-451 3198
Fax. +358-9-451 3195

ISBN 978-951-22-9218-9 (PDF)
ISSN 1459-7268 (PDF)
URL: http://lib.tkk.fi/Reports/2008/isbn9789512292189.pdf

Multiprint Oy
Espoo 2008

HELSINKI UNIVERSITY OF TECHNOLOGY
PO Box 1000, FI - 02015 TKK
http://www.tkk.fi/

ABSTRACT

Faculty
Faculty of Information and Natural Sciences

Department
Department of Engineering Physics

Author(s)
Iwao Nitta, Suvi Karvonen, Olli Himanen & Mikko Mikkola

Title
Modeling the Effect of Inhomogeneous Compression of GDL on Local Transport Phenomena in a PEM Fuel Cell

Abstract

The effects of inhomogeneous compression of gas diffusion layers (GDLs) on local transport phenomena within a polymer electrolyte membrane (PEM) fuel cell were studied theoretically. The inhomogeneous compression induced by the rib/channel structure of the flow field plate causes partial deformation of the GDLs and significantly affects material parameters. The results suggest that inhomogeneous compression does not significantly affect the polarization behavior or gas-phase mass transport. However, the effect of inhomogeneous compression on the current density distribution is evident. Local current density under the channel was substantially smaller than under the rib when inhomogeneous compression was taken into account, while the current density distribution was fairly uniform for the model which excluded the effect of inhomogeneous compression. This is caused by the changes in the selective current path, which is determined by the combinations of conductivities of components and contact resistance between them. Despite the highly uneven current distribution and variation in material parameters as a function of GDL thickness, the temperature profile was relatively even over the active area for both modeled cases, contrary to predictions in previous studies. However, an abnormally high current density significantly accelerates deterioration of the membrane and is critical in terms of cell durability. Therefore, fuel cells should be carefully designed to minimize the harmful effects of inhomogeneous compression.

Keywords (and classification)
Inhomogeneous compression; Gas diffusion layer; PEM Fuel cell; Mathematical model

Place	Month - Year	Language	Number of pages
Espoo, Finland	February 2008	English	23

ISBN (print)	ISBN (electronic)	ISSN (print)	ISSN (electronic)
	978-951-22-9218-9		1459-7268

Serial name
Helsinki University of Technology Publications in Engineering Physics

Serial number or report code
TTK-F-A854

Distribution of the printed publication

Internet access (URL)
http://lib.tkk.fi/Reports/2008/isbn9789512292189.pdf

Table of Contents

1 Introduction

The proton exchange membrane (PEM) fuel cell has been receiving substantial attention as a potential power source for a wide range of applications because of its lower operation temperature compared to other types of fuel cell, flexibility in size, quick start, environmental friendly characteristics and high energy density. However, further improvements of its performance, life-time and cost-effectiveness are still needed to achieve a large-scale commercialization and a deeper understanding of local phenomena taking place in the fuel cell is of vital importance for future development.

A mathematical model is a powerful tool for studying the various phenomena occurring in a fuel cell from local to system level. An excellent review of fuel cell models is given by Yao et al. [1]. The accuracy of the modeled results depends highly on the used modeling parameters and assumptions. Therefore, the experimental evaluation of the physical parameters used in the models is essential. The properties of gas diffusion layers (GDLs) play an especially important role in fuel cell operation [2] and many experimental studies can be found on subjects such as gas permeability [3-8], electrical properties [9-14], thermal properties [15-17], water transport properties [18-28] and the effect of compression [17,29-32]. In accordance with the experimental studies, significant modeling efforts have been devoted to exploring the impact of these parameters on the transport mechanisms and fuel cell performance. Examples of the systematic parametric study are found on the electric anisotropy of GDL [33-35], the thickness and porosity of the GDL [36-39], pore size distribution [40-42], gas permeability [33,43,44], water transport parameters [45-49], and the effect of compression [50-53].

One of the most common shortcomings in previous modeling studies is that the effect of inhomogeneous compression on the GDL induced by the rib/channel structure of the flow field plate was not properly considered. A typical carbon paper or cloth GDL is soft and flexible and therefore, when the GDL is compressed between two flow field plates it is deformed and intrudes in to the channel as shown in Fig. 1. The variations in the GDL thickness and porosity due to compression affect the local transport phenomena since gas permeability, electric conductivity, and electric and thermal contact resistances at the interfaces with neighboring components all depend on compression.

To the authors' knowledge, only a few studies which consider this inhomogeneous compression can be found in literature, see, e.g. [53-56]. Although their findings are enlightening, many of the adopted modeling parameters are subject to a large uncertainty. Therefore, the authors have experimentally evaluated the physical properties of GDL as a function of compressed GDL thickness [57-59] as well as conducted a modeling study using the experimental data [60]. In this paper, the earlier model is improved by applying a more realistic geometry of GDL deformation and the inclusion of thin contact resistance layers with newly evaluated physical parameters as well as correcting some inaccuracies. However, due to a lack of information, particularly for those which describe liquid water behavior, the model excludes two-phase phenomena and the study on the subject is left for future work.

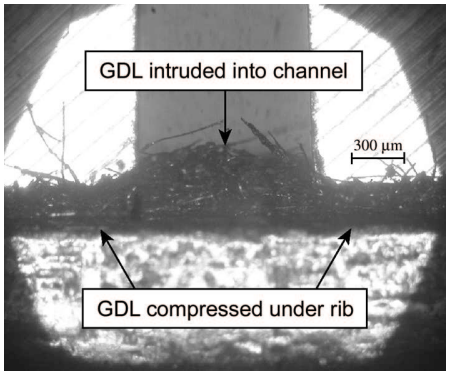

Fig. 1 Cross-sectional view of the GDL (SGL 10 BA, SIGRACET®) taken by optical microscope (PMG3, OLYMPUS).

2 Model description

2.1 Model assumptions

Making a theoretically rigorous fuel cell model which reflects micro- and macro-scale transport processes is extremely challenging because of a lack of experimentally evaluated physical parameters. Therefore, the following assumptions were employed in the model:

(1) Steady state conditions

(2) All gases obey the ideal gas law and are ideally mixed

(3) Water exists only in gaseous form

(4) Very fast reaction kinetics and small mass transfer limitations at the anode

(5) The catalyst layers (CLs) and membrane are isotropic and homogeneous

(6) The membrane is fully hydrated

(7) Physical properties of GDL under the rib are constant

Because of assumption (3), the model presented here is valid only when the partial pressure of water is below the saturation pressure. Assumption (4) implies that the conservation equations for mass, momentum and species at anode GDL and CL are not solved. Assumption (7) was made since all the experimental work to evaluate the physical properties of GDL was conducted by changing the thickness of the compressed GDL under the assumption that the compression pressure applied to the GDL was uniform [57-59].

2.2 Modeling domain

The modeled domain is a two-dimensional partial cross-section of a unit cell as shown in Fig. 2, which consists of a half of both the graphite rib and the channel in the flow field plate, two GDLs and CLs, the electrolyte membrane and pseudo two thin layers TH1 and TH2 which represent the contact resistance between graphite rib and GDL, and GDL and CL, respectively.

The effects of inhomogeneous compression are studied by comparing two models. In the base case, Fig. 2(a), the GDL is compressed evenly and its physical properties are assumed constant. The alternative model, Fig. 2(b), considers the inhomogeneous compression of GDL and the GDL partially intrudes into the flow channel. The shape of the deformed GDL and the dependence of physical properties on the local thickness are described in sub-chapter 2.4.

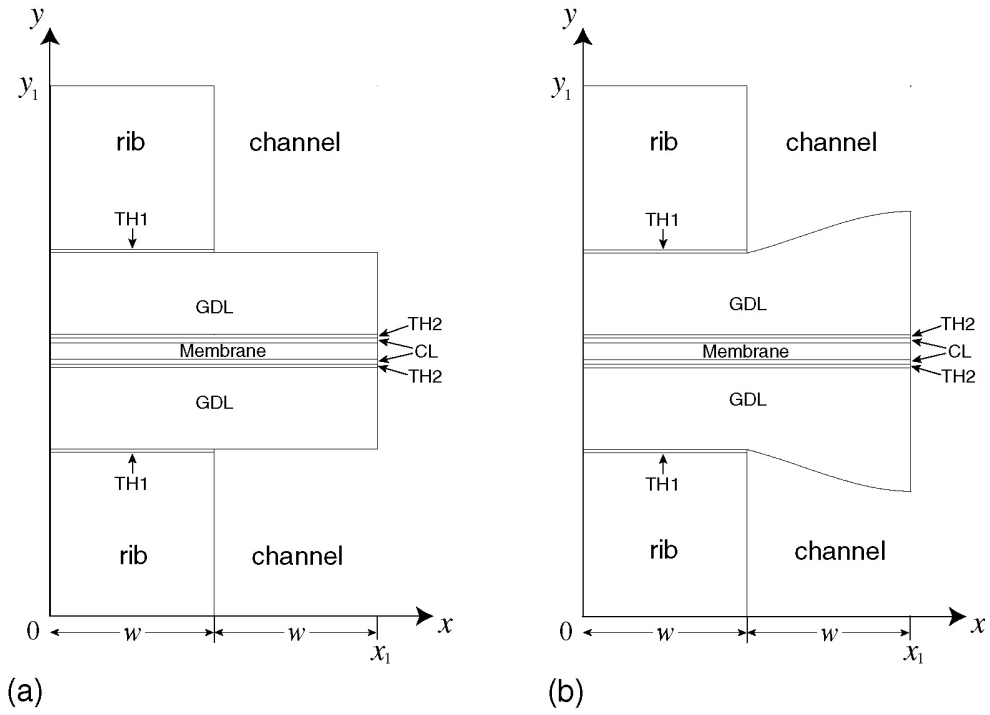

Fig.2 Modeled domain (a) base case, (b) inhomogeneous compression.

2.3 Equations

2.3.1 Governing equations and source terms

The transport phenomena occurring within the cell are modeled with conservation equations for mass, momentum, species, charge and energy. All the governing equations are listed in Table 1. Table 1 also includes the subdomains where the equations are solved.

The Navier-Stokes equation that describes momentum conservation was reduced to Darcy's law since the Reynolds number is less than one and thus the inertia and viscous terms can be neglected in the GDL and CL. Darcy's law was combined with the mass conservation equation which gives Eq. (1) in Table 1. The species conservation equation Eq. (2) is the Maxwell-Stefan diffusion equation and takes into account the convective and diffusive molar fluxes. Since air is fed to the cathode, the multicomponent mass transfer involves a ternary gas mixture (oxygen, water vapor and nitrogen). The charge conservations Eqs. (3 and 4) describe electric current in electrically conductive components and ionic current in ionic conductive components. The energy conservation Eq. (5) takes into account both conductive and convective heat fluxes. Note that on the anode only the charge and energy conservation equations were solved.

Table 1 Governing equations

	Conservation equation		Subdomains
Mass	$\nabla\cdot\left(-\rho_t\frac{k_{sd}}{\mu_t}\nabla p\right)=S_c$	(1)	cathode (GDL, TH2, CL)
Species	$\nabla\cdot\mathbf{N}_i=\nabla\cdot(c_t\mathbf{v}X_i)-\nabla\cdot(c_t\overline{D}_{eff}\nabla X_i)=S_i$	(2)	cathode (GDL, TH2, CL)
Charge (electric)	$\nabla\cdot(-\sigma_{s,sd}\nabla\phi_s)=S_s$	(3)	rib, TH1, GDL, TH2, CL
(ionic)	$\nabla\cdot(-\sigma_{m,sd}\nabla\phi_m)=S_m$	(4)	CL, membrane
Energy	$\nabla\cdot\left(\sum_i\rho_i C_{p,i}\mathbf{v}T\right)-\nabla\cdot(\kappa_{sd}\nabla T)=S_T$	(5)	all

The source terms for the governing equations are listed in Table 2. The source terms of the mass and species conservation equation represent the consumption of oxygen and production of water in the cathode CL. The number of electrons involved in the reaction (4 for oxygen consumption, 2 for water production) appears in these equations. The source terms in the charge conservation equation describe the charge transfer current density between the electric and ionic phases inside the anode and cathode CLs. The transfer current densities are expressed with the Butler-Volmer relation as follows:

$$j_a=-a_v j_a^{ref}\left[\frac{(\alpha_a^a+\alpha_c^a)F}{RT}\eta_a\right] \quad \text{for anode} \quad (6)$$

$$j_c=a_v j_c^{ref,T}\left(\frac{c_{O_2}}{c_{O_2}^{ref}}\right)\exp\left(-\frac{\alpha_c^c F}{RT}\eta_c\right) \quad \text{for cathode} \quad (7)$$

Anode side has fast reaction kinetics and low overpotential compared to the cathode, and thus anode transfer current density can be linearized as in Eq. (6). The reference concentration $c_{O_2}^{ref}$ is equal to the concentration of oxygen in air at STP conditions and c_{O_2} is the concentration of oxygen in the CL. In the model, the ratio of c_{O_2} to $c_{O_2}^{ref}$ in Eq. (7), was replaced by the molar fraction of oxygen, X_{O_2} . η_a and η_c are the overpotentials at anode and cathode, respectively:

$$\eta_a=\phi_m-\phi_{s,a} \quad (8)$$

$$\eta_c=\phi_{s,c}-\phi_m-E_0 \quad (9)$$

where E_0 is the open circuit voltage.

The source terms in the energy conservation equation correspond to Joule heating, irreversible heat of electrochemical reactions and entropic heat of reactions in CLs but only Joule heating in other subdomains.

Table 2 Source terms in each modeling subdomain.

Region	Mass	Species	Charge	Energy
GDL	0	0	0	$S_T = \sigma_{GDL}(\nabla\phi_s)^2$
CL				
(Anode)	0	0	$S_{s,a} = -j_a$ $S_{m,a} = j_a$	$S_T = \sigma_s^{CL}(\nabla\phi_s)^2 + \sigma_m^{CL}(\nabla\phi_m)^2 + j_a\eta_a + \frac{j_a T\Delta S_a}{2F}$
(Cathode)	$S_c = -\frac{j_c M_{O_2}}{4F} + \frac{j_c M_{H_2O}}{2F}$	$S_{O_2} = -\frac{j_c}{4F}$ $S_{H_2O} = \frac{j_c}{2F}$	$S_{s,c} = j_c$ $S_{m,c} = -j_c$	$S_T = \sigma_s^{CL}(\nabla\phi_s)^2 + \sigma_m^{CL}(\nabla\phi_m)^2 - j_c\eta_c - \frac{j_c T\Delta S_c}{4F}$
TH1, TH2	0	0	0	$S_T = \sigma_{s,sd}(\nabla\phi_s)^2$
Membrane	0	0	0	$S_T = \sigma_m(\nabla\phi_m)^2$

The constitutive relations used for the governing equations are listed in Table 3. The molar density can be calculated from ideal gas law as in Eq. (10). The molar fraction of nitrogen is calculated from the fact that the sum of molar fractions is equal to unity Eq. (11). The effective Maxwell-Stefan diffusion coefficient tensor, $\overline{D}_{eff}$, is related to the non-porous diffusion coefficient, $\overline{D}$, through the Bruggeman correlation as in Eq. (12). The elements of the $\overline{D}$ for a ternary system are calculated from the Maxwell-Stefan binary diffusion coefficients as in Eq. (13). The temperature and pressure dependence of the binary diffusion coefficients was taken into account with Eq. (14). Also, the temperature dependence of exchange current density was taken into account with Eq. (15).

Table 3Constitutive relations.

Expression		
Ideal gas law	$\rho_t = M_t c_t = \frac{M_t p}{\Re T}$	(10)
Molar mass of gas mixture	$M_t = \sum_i X_i M_i$	(11)
Effective diffusion coefficient tensor	$\overline{D}_{eff} = \varepsilon_{sd}^{1.5}\overline{D}$	(12)
Elements of $\overline{D}$	$D_{11} = D_{O_2,N_2}\frac{X_{O_2}D_{H_2O,N_2} + (1-X_{O_2})D_{O_2,H_2O}}{S}$ $D_{12} = X_{O_2}D_{H_2O,N_2}\frac{D_{O_2,N_2} - D_{O_2,H_2O}}{S}$ $D_{21} = X_{H_2O}D_{O_2,N_2}\frac{D_{H_2O,N_2} - D_{O_2,H_2O}}{S}$ $D_{22} = D_{H_2O,N_2}\frac{X_{H_2O}D_{O_2,N_2} + (1-X_{H_2O})D_{O_2,H_2O}}{S}$ $S = X_{O_2}D_{H_2O,N_2} + X_{H_2O}D_{O_2,N_2} + X_{N_2}D_{O_2,H_2O}$	(13)
Temperature and pressure dependence of binary diffusion coefficients	$D_{i,j} = \frac{p_0}{p}\left(\frac{T}{T_0}\right)^{1.5} D_{i,j}(p_0, T_0)$	(14)
Temperature dependence of exchange current density	$j_c^{ref,T} = j_c^{ref,T_0}\exp\left[-\frac{\Delta E_{exc}}{\Re}\left(\frac{1}{T} - \frac{1}{T_0}\right)\right]$	(15)

2.3.2 Boundary conditions

Symmetry boundary conditions were applied at $x = 0$ and $x = x_1$ in Fig. 2, i.e. all the fluxes were set to zero. No electric current passes through the interface between the GDL/channel and CL/membrane. It was assumed that there is no ionic contact resistance at the CL/membrane interface, and thus the ionic potential and temperature are continuous. On the other hand, ionic current does not pass through the GDL/CL interface since the GDL is not ionically conductive. The concentrations and pressure are continuous through GDL, TH2 and CL, and no boundary conditions are required at the interfaces. However, there is no mass flux across the rib/GDL and CL/membrane interfaces.

At the cathode gas channel/GDL interface, the pressure was set equal to ambient pressure. The molar fractions of the species at the channel/GDL interface were calculated based on the following assumptions

(1) The modeled cross-section is in the middle of cell and produced current is constant along the channel.

(2) The stoichiometry of air is 2

(3) The air temperature is 325 K and the relative humidity or the air is 40%.

(4) There is no water transport through the membrane

Thus the molar fractions of oxygen and water vapor were fixed to 0.143 and 0.149, respectively.

Furthermore, heat transfer from the GDL to air in the channel is calculated via:

$$-\mathbf{n}\cdot\mathbf{Q} = \kappa_h\left(T_{GDL} - T_{air}\right) \tag{16}$$

where $\mathbf{Q}$ denotes the heat flux calculated from Eq. (5), κ_h the heat transfer coefficient, T_{GDL} the temperature of GDL and T_{air} the temperature of air. The temperature of the graphite ribs at $y = 0$ and $y = y_1$ was set to 330 K.

The electric and thermal contact resistances at graphite rib/GDL and GDL/CL interfaces were converted to corresponding electric and thermal conductivities of TH1 and TH2. Therefore, the electric potential and temperature through graphite rib, GDL and CL are continuous through the TH1 and TH2 and no boundary conditions have to be prescribed.

2.4 Model input parameters

Table 4 lists the cell design parameters and material, kinetic and electrochemical parameters. When the GDL deformation is taken into account (see Fig. 2b), the properties of GDL are varied as a function of the thickness. These changes are described in the following sub-chapters.

2.4.1 GDL deformation

The deformation curve of GDL observed in the photomicrographs taken with an optical microscope (Fig. 1) was fitted with a third order polynomial (fitting accuracy: $R^2 = 0.947$) and its dimensionless thickness can be expressed as:

$$h(x) = \begin{cases} h_c \text{ m}^{-1}, & x \le 500\times10^{-6} \text{ m} \\ -1.047 \text{ m}^{-3}x^3\times10^6 + 2.105 \text{ m}^{-2}x^2\times10^3 - 1.070 \text{ m}^{-1}x + 3.894\times10^{-4}, & x > 500\times10^{-6} \text{ m} \end{cases} \tag{17}$$

for the case where the compressed GDL thickness, h_c, is 250 μm. The same process was used to obtain expressions for the thickness of the GDL when the h_c was varied from 150 to 300 μm.

2.4.2 Gas permeability and porosity

The reduction of the GDL thickness was assumed to be caused by the reduction of GDL porosity. Therefore, the porosity of the compressed GDL, ε_c, is calculated from the equation, see, e.g [5]

$$\varepsilon_c = \frac{h(x) - h_s}{h(x)} = 1 - (1 - \varepsilon_0)\frac{h_0}{h(x)} \tag{18}$$

where ε_0 denotes the porosity of uncompressed GDL and h_0 the thickness of uncompressed GDL. h_s is the thickness of the GDL when all the pores are lost:

$$h_s = (1 - \varepsilon_0)h_0 \tag{19}$$

The reduction of GDL porosity leads into a decrease in gas permeability. The gas permeability of the compressed GDL, $k(x)$, was evaluated [57] and the fitted curve (fitting accuracy: $R^2 = 0.997$) can be expressed as

$$k(x) = 0.806h(x)^3 - 6.464\times10^{-5}h(x)^2 - 5.305\times10^{-8}h(x) + 7.164\times10^{-12} \text{ [m}^2\text{]} \tag{20}$$

The porosity of CL, ε_{CL}, adopted by Bernardi et al. [61] and permeability of CL, k_{CL}, reported by Himanen et al. [62] were assumed to be not affected by compression.

2.4.3 Electric properties

The electric conductivity of the GDL as a function of compressed GDL thickness was evaluated in a previous study [57]. The conductivity was found to be anisotropic and fitted with a linear curve (fitting accuracy: $R^2 = 0.964$ for in-plane and $R^2 = 0.975$ for through-plane):

$$\sigma_{\text{GDL,x}} = -1.159\times10^7 h(x) + 6.896\times10^3 \text{ [S m}^{-1}\text{]} \qquad \text{for in-plane conductivity} \tag{21}$$

$$\sigma_{\text{GDL,y}} = -8.385\times10^6 h(x) + 3.285\times10^3 \text{ [S m}^{-1}\text{]} \qquad \text{for through-plane conductivity} \tag{22}$$

The electric contact resistances between the GDL and other cell components depend strongly on the compression pressure. The electric contact resistance between GDL and graphite current collector, $R_{\text{c,GDL/GR}}(h_c)$ was found to decrease exponentially as GDL was compressed [57]. The $R_{\text{c,GDL/GR}}(h_c)$ was converted into through-plane electric conductivity of TH1, $\sigma_{\text{TH1,y}}(x)$. The $\sigma_{\text{TH1,y}}(x)$ was calculated as a function of compressed GDL thickness, and exponential curve was fitted into the data (fitting accuracy: $R^2 = 0.983$), yielding:

$$\sigma_{TH1,y}(x) = 1.714\times10^4 \exp\left[-2.056\times10^4 h_c\right] \text{ [S m}^{-1}\text{]} \tag{23}$$

The electric contact resistance between the GDL and CL, $R_{\text{c,GDL/CL}}(h_c)$, was also evaluated experimentally by the authors [59]. The $R_{\text{c,GDL/CL}}(h_c)$ was converted to the through-plane electric conductivity of TH2, $\sigma_{\text{TH2,y}}(x)$, which was fitted with a third degree polynomial (fitting accuracy: $R^2 = 0.996$), giving

$$\sigma_{TH2,y}(x) = 7.726\times10^{11} h(x)^3 - 4.943\times10^8 h(x)^2 + 2.664\times10^4 h(x) + 18.911 \text{ [S m}^{-1}\text{]} \tag{24}$$

Accurate experimental evaluation of the $R_{\text{c,GDL/CL}}(h_c)$ was found difficult as the compression pressure decreased. Therefore, in ref. [59], the lowest compression pressure at which the $R_{\text{c,GDL/CL}}(h_c)$ could be evaluated was 0.664 MPa. This corresponds to a GDL thickness of approximately 300 μm, above which the accuracy of Eq. (24) diminishes. However, the trend is clear – the lower the compression, the higher the contact resistance.

It should be noted that the values used for the in-plane electric conductivity of TH1 and TH2, $\sigma_{\text{TH1,x}}$ and $\sigma_{\text{TH2,x}}$, were set equal to the in-plane electric conductivity of GDL and CL, respectively. These values were adopted because the lateral current flow in the TH1 and TH2 can be expected to follow to that in the neighboring more conductive components, the GDL and CL. On the other hand, the conductivity of CL evaluated previously [57] was assumed to be isotropic since no reliable experimental data on its anisotropy was found.

2.4.4 Thermal properties

Compared to electric properties, relatively little experimental data on the thermal properties of GDL have been reported in the literature. According to the authors' previous study [58], the through-plane thermal conductivity of GDL, κ_{GDL}, was not affected by the compression pressure and a constant value was used in this model. The in-plane thermal conductivity of GDL was assumed to be the same as the through-plane thermal conductivity.

The evaluated thermal contact resistance between the graphite current collector and GDL [58] was converted to the through-plane thermal conductivity of TH1, $\kappa_{TH1,y}(x)$. The calculated $\kappa_{TH1,y}(x)$ as a function of compressed GDL thickness was fitted with a fourth degree polynomial (fitting accuracy: $R^2 = 0.993$), giving

$$\kappa_{TH1,y}(x) = -2.912\times10^{14}\,h(x)^4 + 3.133\times10^{11}\,h(x)^3 - 1.170\times10^{8}\,h(x)^2 + 1.639\times10^{4}\,h(x) - 0.438 \ [\mathrm{W\ m^{-1}\ K^{-1}}] \quad (25)$$

The thermal contact resistance between the GDL and CL was assumed to be same as the thermal contact resistance between graphite and GDL. Therefore, Eq. (25) was used also for the through-plane thermal conductivity of TH2, $\kappa_{TH2,y}(x)$. The in-plane thermal conductivities of TH1 and TH2, $\kappa_{TH1,x}$ and $\kappa_{TH2,x}$, were set equal to the in-plane thermal conductivity of GDL and CL, respectively, based on the same assumption of charge transport at the interface.

The thermal conductivity of CL was calculated from the data reported by Khandelwal et al. [15]. In their study, the combined thermal resistance, i.e. thermal bulk resistance of the CL plus thermal contact resistance between GDL and CL, was determined to be 1.25×10^{4} m^2 K W^{-1} at a compression pressure of 1.83 MPa (compressed GDL thickness of ca. 250 µm [58]). By subtracting the thermal contact resistance between GDL and CL, which can be calculated from Eq. (25), from the combined thermal resistance, the thermal bulk resistance of CL was determined. The thermal conductivity of CL, κ_{CL}, calculated using the measured thermal bulk resistance of CL was assumed to be isotropic and independent of compression.

Table 4 Cell design parameters and material properties.

Symbol	Description	Value
Geometrical parameters		
w	Channel and rib width	500 µm
h_c	Compressed GDL thickness under rib	150–300 µm
h_0	Uncompressed GDL thickness	380 µm
	CL thickness	25 µm
	Membrane thickness	50 µm
	TH1, TH2 thickness	10 µm

Table 4 Continued…

Symbol	Description		Value
Material parameters			
$D_{O_2,H_2O}(p_0,T_0)$	diffusion coefficient O_2,H_2O		3.98×10^{-5} m^2 s^{-1} [60]
$D_{O_2,N_2}(p_0,T_0)$	Binary diffusion coefficient O_2,N_2		2.95×10^{-5} m^2 s^{-1} [60]
$D_{H_2O,N_2}(p_0,T_0)$	Binary diffusion coefficient H_2O,N_2		4.16×10^{-5} m^2 s^{-1} [60]
σ_s^{CL}	CL electric conductivity		320 S m^{-1} [57]
σ_m^{CL}	CL ionic conductivity		5.09 S m^{-1}
κ_{CL}	CL thermal conductivity		0.476 W m^{-1} K^{-1} [15]
κ_{GDL}	GDL thermal conductivity		1.18 [58]
σ_{GR}	Graphite plate electric conductivity		69700 S m^{-1} [63]
κ_{GR}	Graphite plate thermal conductivity		128 W m^{-1} K^{-1} [63]
σ_{m}	Membrane ionic conductivity		5.09 S m^{-1} [64]
κ_{m}	Membrane thermal conductivity		0.12 W m^{-1} K^{-1} [15]
κ_{h}	Heat transfer coefficient from GDL to air		5 W m^{-2} K^{-1}
k_{CL}	Permeability of CL		1.26×10^{-13} m^2 [62]
ε_0	Porosity of uncompressed GDL		0.83 [65]
$\varepsilon_{\mathrm{CL}}$	Porosity of CL		0.4 [61]
Kinetic and electrochemical and other parameters			
ΔE_{exc}	Activation energy	($E_{cell} \geq 0.8$V)	76.5 kJ mol^{-1} [66]
		($E_{cell} < 0.8$V)	27.7 kJ mol^{-1} [66]
p_0	Ambient pressure		101 325 Pa
$\alpha_a^a + \alpha_c^a$	Anodic and cathodic transfer coefficients in Eq. (33)		1 [34]
α_c^c	Cathodic transfer coefficient in Eq. (34)		1 [34]
ΔS_{a}	Entropy change of anode		0.104 J mol^{-1} K^{-1}
ΔS_{c}	Entropy change of cathode		-326.36 J mol^{-1} K^{-1}
$a_v j_a^{ref}$	Exchange current density × ratio of reaction surface to CL volume, anode		1.7×10^9 A m^{-3} [60]
$a_v j_c^{ref,T_0}$	Exchange current density × ratio of reaction surface to CL volume, cathode		2×10^4 A m^{-3} [60]
C_{p,O_2}	Heat capacity of oxygen		923 J kg^{-1} K^{-1}
C_{p,H_2O}	Heat capacity of water vapor		1996 J kg^{-1} K^{-1}
E_0	Open circuit voltage		1.23 V
T_0	Reference temperature		273 K

3 Results and discussion

3.1 Polarization behavior and species distribution

In the following discussion of modeling results, the compressed GDL thickness under the rib is 250 µm for the both cases, i.e. base case and case considering inhomogeneous compression, unless stated otherwise.

The polarization curves for the two modeled cases, presented in Fig. 3, were obtained by changing the cell voltage from 1 to 0.45 V. The curves are almost identical for both the cases except at lower voltages. Since two-phase flow is not taken into account here, the model is valid only when partial pressure of water, p_{H_2O}, does not exceed the saturation pressure, p_{sat}. The lowest limit for voltage was determined by calculating the relative humidity under the rib where flooding usually starts, see e.g. [67]. Fig. 4 shows the relative humidity of gas (p_{H_2O} / p_{sat}) at the GDL/CL interface at cell voltages of 0.45 and 0.5 V. In both modeled cases, water starts to condense when the cell voltage is below 0.5 V. In the following, therefore, the cell voltage is fixed to 0.5 V.

Fig. 5 shows the molar fraction of oxygen at the GDL/CL interface for both the modeled cases. Only slight difference in molar fraction of oxygen is observed between the two cases as discussed in previous work [60], which suggests that the mass transfer is not significantly affected by GDL deformation as long as no flooding occurs.

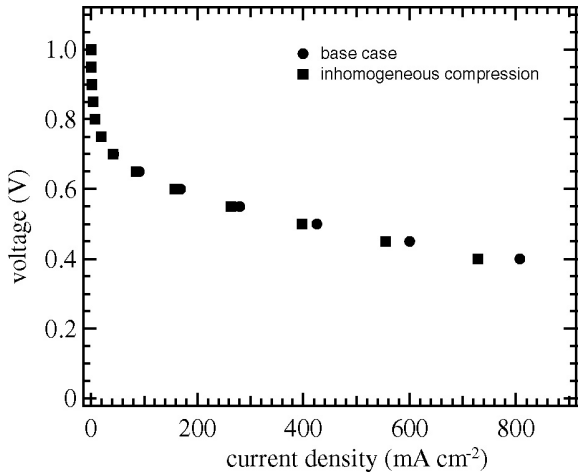

Fig. 3 Polarization curves for the base case and case considering the inhomogeneous compression.

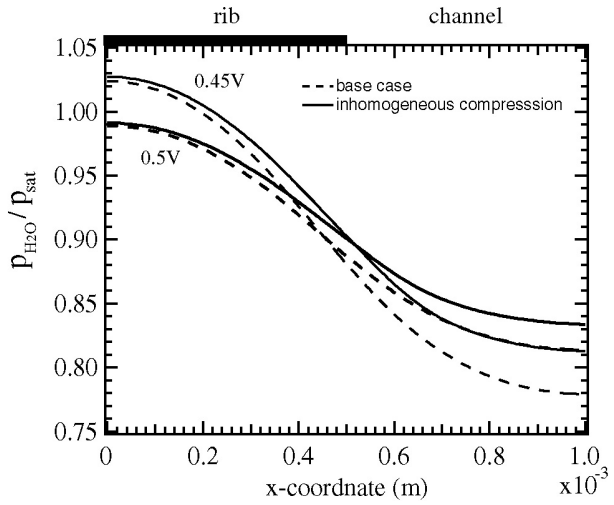

Fig. 4 Relative humidity (p_{H2O}/p_{sat}) at the GDL/CL interface at the cell voltage of 0.45 (thin line) and 0.5 V (bold line) for the base case and case considering the inhomogeneous compression.

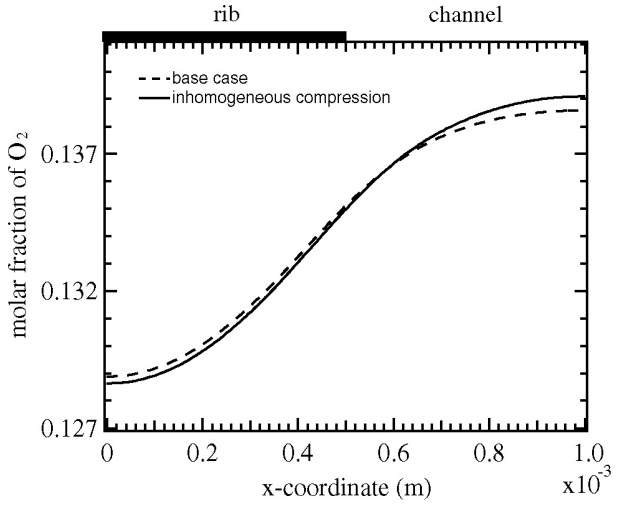

Fig. 5 Oxygen molar fraction at the GDL/CL interface at cell voltage of 0.5 V.

3.2 Current density distribution

Fig. 6 shows the current density distribution at the GDL/CL interface. For the base case, the current density distribution is fairly uniform over the active area. However, a notably uneven distribution is seen when inhomogeneous compression is taken into account. In this case the local current density is significantly lower in the middle of the channel and increases in the region close to the edge of the rib. This is because of changes in the selective current path, which is largely determined by the electric contact resistance between the GDL and CL, i.e. $\sigma_{TH2,y}(x)$ in Eq. (24), and electric conductivities of GDL in Eqs. (21 and 22). A large portion of the produced current flows laterally under the channel where the contact resistance is high and crosses over to the GDL near the rib edge (see Fig. 7).

The shape of the current density distribution is different from that observed in the previous study [60]. The difference mainly arises from the estimates used for the contact resistance between the GDL and CL, and the shape of the deformed GDL, which both differed significantly from the experimentally evaluated values used here. As a result, the current density was overestimated at the edge of the rib and under the channel in the previous study.

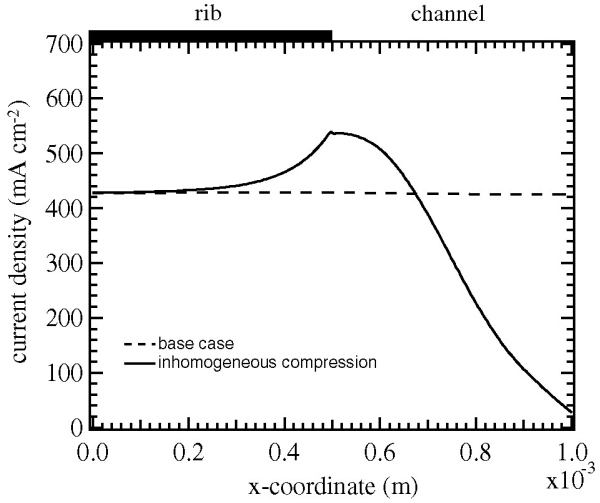

Fig. 6 Current density distribution at the GDL/CL interface at cell voltage of 0.5 V.

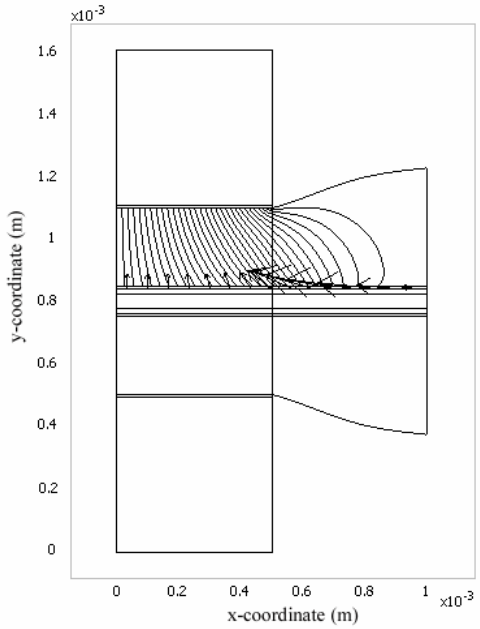

Fig. 7 Current density profile at TH2/CL interface (arrow plot) and at cathode GDL (streamline plot). Note that the magnitudes of arrow and streamline plots are not in scale.

3.3 Temperature profile

Fig. 8 shows the temperature profile at the GDL/CL interface. It is interesting to note that when inhomogeneous compression is taken into account the temperature profile is more uniform than that of the base case. A possible reason for this is that the current density under the channel is substantially smaller when inhomogeneous compression is taken into account than in the base case (see Fig. 6). All the terms of the heat source equation include current density, and thus the current density distribution directly affects the temperature profile. Among the heat sources, the irreversible heat of electrochemical reactions accounts for a major part of heat production.

The temperature difference across the active area for the case considering inhomogeneous compression, less than 1 ˚C, is much smaller than the value, more than 10 ˚C, predicted in a previous study [68]. There, the values for the thermal contact and thermal bulk resistances were overestimated and the values of electric contact resistance between GDL and CL were underestimated, leading into larger temperature differences across the components.

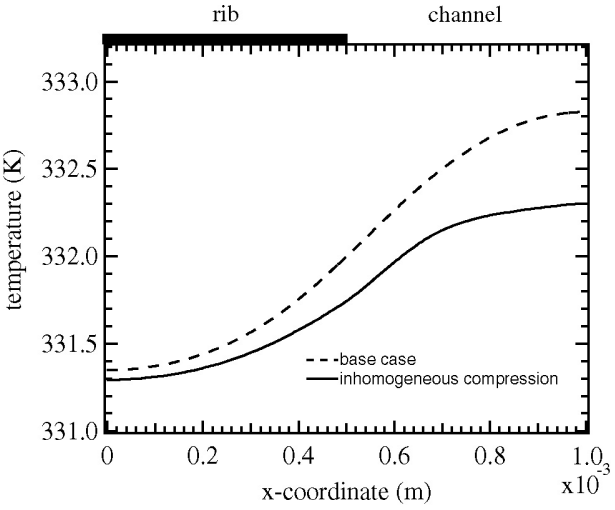

Fig. 8 Temperature distribution at the GDL/CL interface at cell voltage of 0.5 V.

3.4 Effect of the compressed GDL thickness

Applying the simulation technique described above, the effects of compressed GDL thickness on charge and heat transport were investigated. The thickness of the compressed GDL under the rib was varied from 300 to 150 μm, and a corresponding expression for the shape of the GDL intruding into the channel was used. The physical properties of the GDL were changed correspondingly.

Fig. 9(a) shows the current density distribution at the GDL/CL interface for various compressed GDL thicknesses under the rib. The total current integrated over the active area increases as the GDL is compressed more, since both the electric contact and bulk resistances of GDL are reduced. For example, the case in which the GDL is compressed to 150 μm produces ca. 25% more current than the case of 300 μm at the same cell voltage of 0.5 V. The shape of the current density distribution also changes when the compressed GDL thickness is changed. A current density peak is observed at the edge of the rib when the GDL is compressed to 300 μm. On the other hand, when the GDL under the rib is compressed to 150 μm the current density has a maximum at around x = 0.61 mm. In this case, the contact resistance between GDL and CL is small enough even under the channel so that lateral current flows in the CL change the direction and enter into the GDL. The shape of current density distribution is largely determined by the profile of the deformed GDL, on which the contact resistance between the GDL and CL depends.

Fig. 9(b) shows the temperature profile at the GDL/CL interface for various compressed GDL thicknesses under the rib. As predicted in the previous study [58], the temperature under the rib increases with decreasing compression because of an increase in both thermal bulk and contact resistance. However, the temperature profile becomes more uniform over the active area when the GDL under the rib is less compressed. This is due to the lower heat production under the channel in such a case. Since the value of oxygen molar fraction depends on the porosity of GDL, i.e. the shape of GDL, lower compression of GDL leads into relatively higher value of oxygen molar fraction compared to the case of higher compression, which in turn results in a lower value of overpotential in CL. Even though the differences in their values are fairly small (ca. less than 2% for both oxygen molar fraction and overpotential), changes in heat production are notable. For example, the irreversible heat of electrochemical reactions when the compressed GDL thickness is 200 μm is ca. 23% higher than that for the case of 300 μm on an average over the active area.

The minor irregularities in the shape of the current density distribution under the channel (Fig. 9(a)), such as variation in the value of current density in the middle of the channel and crossing of the current density curves for the GDLs compressed to 150 and 200 μm at around x = 0.81 mm, stems from the difficulty of determining the profile of the GDL intrusion into the channel $h(x)$, i.e.

the equivalent of Eq. (17) for each compressed GDL thickness under the rib. Due to the structure of the GDL, the profile of the deformed part and the uncompressed GDL thickness under the channel varied from sample to sample in the photomicrographs taken at the same compressed thickness under the rib. Therefore, the expressions for $h(x)$ are unique for each sample and compressed thickness, which is in turn reflected in the current density profiles.

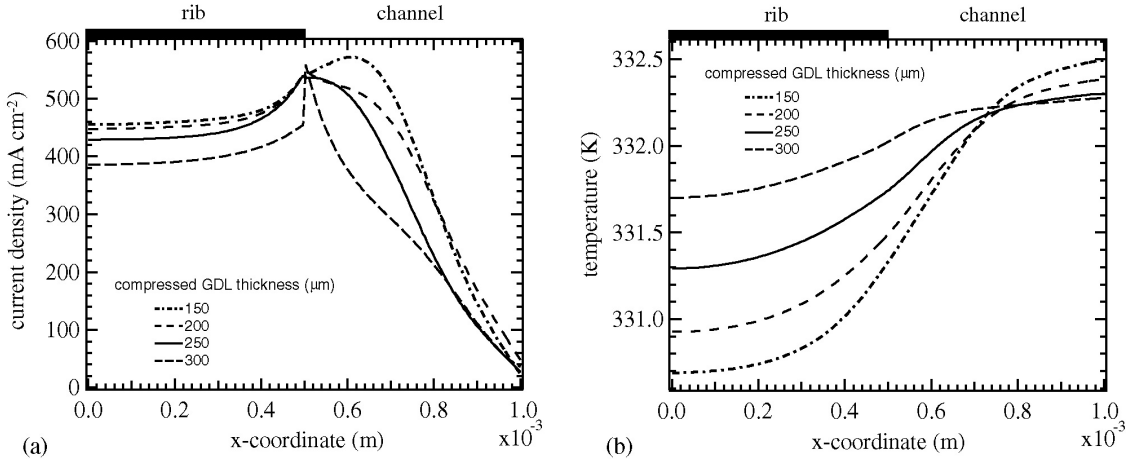

Fig. 9(a) Current density distribution and (b) temperature profile at the GDL/CL interface at cell voltage of 0.5 V with various compressed GDL thickness (150–300 μm) under the rib.

4 Summary and conclusion

A two-dimensional model was developed to study the effect of inhomogeneous compression of GDL on the local transport phenomena in PEM fuel cell. The results were compared to those given by a base case model in which the GDL compression was assumed to be homogeneous.

The polarization behavior and gas-phase mass transport predicted by the two models were almost identical, but the current density profiles were noticeably different. The model which considered the inhomogeneous compression showed that the local current density under the channel was substantially smaller than under the rib and had a maximum at the edge of the rib, while the current density for the base case was fairly uniform over the active area. This high variation in local current density may significantly accelerate membrane deterioration and affect the cell durability.

The model predicted a fairly uniform temperature profile over the active area, with a maximum variation of ca. 1 °C. This contradicts the results of a previous study [68], where a larger temperature variation, up to 10 °C, was predicted within the cell under similar conditions. This difference stems from the adopted modeling parameters such as contact resistance and conductivity, and the geometry of the deformed GDL. Especially the local current density distribution, which significantly affects the temperature profile, was found to be very sensitive to the value and variation of contact resistance between GDL and CL. Therefore, the right choice of modeling parameters is essential for accurate prediction of local phenomena which can not be easily interpreted by the modeled polarization curves only, as discussed in literature [69-71].

The compressed GDL thickness under the rib affects the current density distribution and temperature profile. Although the total current over the active area increased as GDL was compressed more, the unevenness of the temperature profiles became more prominent. Further effort should be made to mitigate the detrimental effects of inhomogeneous compression of GDL, e.g. by developing rigid GDLs or rigid micro porous layers onto the GDL which do not deform under compression, or implementing pre-treatment which curbs or compensates for the deformation of the GDL.

A limitation of the model presented here is that phase change of water and liquid water transport are not considered. When the cell is flooded by the condensed water, gas transport is significantly

hindered, which in turn affects the current production and temperature distribution. A further study using proper water transport parameters is left for the future.

Acknowledgements

The authors gratefully acknowledge the financial support from the Fortum Foundation, the Academy of Finland (decision #110748), the Wihuri Foundation and Tekes, the Finnish Funding Agency for Technology and Innovation.

Nomenclature

a_v ratio of reaction surface to CL volume (m^{-1})

c concentration (mol m^{-3})

C_p heat capacity (J kg^{-1} K^{-1})

D diffusion coefficient (m^2 s^{-1})

F Faraday's constant, 96487 (As mol^{-1})

h thickness (m)

j transfer current density (A m^{-3})

j^{ref} exchange current density (A m^{-2})

k permeability (m^2)

M molar mass (kg mol^{-1})

$\mathbf{n}$ unit vector

$\mathbf{N}$ molar flux (mol $m^{-2}s^{-1}$)

p pressure (Pa)

$\mathbf{Q}$ heat flux (W m^{-2})

R gas constant, 8.314 (J $mol^{-1}K^{-1}$)

S source term

T temperature (K)

$\mathbf{v}$ velocity (m s^{-1})

X molar fraction

Greek letters

α transfer coefficient

ε porosity

η overpotential (V)

κ thermal conductivity (W $m^{-1}K^{-1}$)

μ viscosity of air, 1.9×10^{-5} (kg m^{-1} s^{-1})

ρ density (kg m^{-3})

σ electric conductivity ($\Omega^{-1}m^{-1}$)

ϕ potential (V)

Subscripts

a	anode
c	cathode
CL	catalyst layer
GDL	gas diffusion layer
GR	graphite
H_2O	water
i	species of gas
m	ionic phase
N_2	nitrogen
O_2	oxygen
s	electric phase
sat	saturation
sd	subdomain
t	mixture of gas
TH1	thin layer 1
TH2	thin layer 2
x	x-direction, in-plane
y	y-direction, through-plane

References

1 K.Z Yao, K. Kran, K.B. McAuley, P. Oosthuizen, B. Peppley, T. Xie, Fuel Cell 4 (1) (2004) 3–29.

2 M. Mathias, J. Roth, J. Fleming,W. Lehnert, in:W. Vielstich, A. Lamm, H. Gasteiger (Eds.), Handbook of Fuel Cells, John Wiley & Sons, Ltd., New York, 2003, pp. 517–537.

3 H. Dohle, R. Jung, N. Kimiaie, J. Mergel, M. Müller, J. Power Sources 124 (2003) 371–384.

4 V. Gurau, M.J. Bluemle, E.S. De Castro, Y-M Tsou, T.A. Zawodzinski, J.A. Mann., J. Power Sources 165 (2007) 793–802.

5 J.T. Gostick, M.W. Fowler, M.D. Pritzker, M.A. Ioannidis, L.M. Behra, J. Power Sources 162 (2006) 228–238.

6 J.P. Feser, A.K. Prasad, S.G. Advani, J. Power Sources, 162 (2006) 1226–1231.

7 M.V. Williams, E. Begg, L. Bonville, H.R. Kunz, J.M. Fenton, J. Electrochem. Soc. 151 (8) (2004) A1173–A1180.

8 J. Soler, E. Hontanon, L. Daza, J. Power Sources 118 (2003) 172–178.

9 S.A. Freunberger, M. Reum, J. Evertz, A. Wokaun F.N. Büchia, J. Electrochem. Soc. 153 (2006) A2158–A2165.

10 T. Tomimura, S. Nakamura, H. Nonami, H. Saito, 2001 IEEE 7th International Conference on Solid Dielectrics, (2001) 101–104.

11 V. Mishra, F. Yang, R. Pitchumani, J. Fuel Cell Sci. Technol. 1 (2004) 2–9.

12 J. Ihonen, F. Jaouen, G. Lindbergh, G. Sundholm, Electrochim. Acta 46 (2001) 2899–2911.

13 P. M. Wilde, M. Mandle, M. Murata, N. Berg, Fuel Cells 4 (3) (2004) 180–184.

14 Cunningham, M. Lefévre, G. Lebrun, J.P. Dodelet, J. Power Sources 143 (2005) 93–102.

15 M. Khandelwal, M.M. Mench, J. Power Sources 161 (2006) 1106–1115.

16 P.J.S. Vie, S. Kjelstrup, Electrochim. Acta 49 (2004) 1069–1077.

17 J. Ihonen, M. Mikkola, G. Lindbergh, J. Electrochem. Soc. 151 (8) (2004) A1152–A1161.

18 J.T. Gostick, M.W. Fowler, M.A. Ioannidis, M.D. Pritzker, Y.M. Volfkovich, A. Sakars, J. Power Sources 156 (2006) 375–387.

19 V. Gurau, M.J. Bluemle, E.S.D. Castro, Y-M. Tsou, J.A.Mann Jr., T.A. Zawodzinski Jr., J. Power Sources 160 (2006) 1156–1162.

20 S. Litster, D. Sinton, N. Djilali, J. Power Sources 154 (2006) 95–105.

21 A. Bazylak, D. Sinton, Z.S. Liu, N. Djilali, J. Power Sources 163 (2007) 784–792.

22 N. Holmström, J. Ihonen, A. Lundblad, G. Lindbergh, Fuel Cells 7 (4) (2007) 306–313.

23 J. Benziger, J. Nehlsen, D. Blackwell, T. Brennan, J. Itescu, J. Membrane Science 261 (2005) 98–106.

24 E.C. Kumbur, K.V. Sharp, M.M. Mench, J. Power Sources 161 (2006) 333–345.

25 E.C. Kumbur, K.V. Sharp and M.M. Mench, Journal of Power Sources, In Press, Accepted Manuscript, (2007).

26 E.C. Kumbur, K.V. Sharp, M.M. Mench, J. Electrochem. Soc., 154 (12) B1295–B1304 (2007).

27 E.C. Kumbur, K.V. Sharp, M.M. Mench, J. Electrochem. Soc., 154 (12) B1305–B1314 (2007).

28 E.C. Kumbur, K.V. Sharp, M.M. Mench, 54 (12) B1315–B1324 (2007).

29 W.K. Lee, C.H. Ho, J.W.V. Zee, M. Murthy, J. Power Sources 84 (1999) 45–51.

30 J. Ge, A. Higier, H. Liu, J. Power Sources 159 (2006) 922–927.

31 S. Escribano, J.F. Blachot, J. Etheve, A. Morin, R. Mosdale, J. Power Sources 156 (2006) 8–13.

32 W.R. Chang, J.J. Hwang, F.B. Weng, S.H. Chan, J. Power Sources 166 (2007) 149–154.

33 J.G. Pharoah, K. Karan, W. Sun, J. Power Sources 161 (2006) 214-224.

34 T. Zhou, H. Liu, J. Power Sources 161 (2006) 444–453.

35 H. Meng, C.Y. Wang, J. Electrochem. Soc. 151 (2004) A358-A367.

36 J.H. Jang, W.M. Yan, C.C. Shih, J. Power Sources 156 (2006) 244–252.

37 G. Inoue, Y. Matsukuma, M. Minemoto, J. Power Sources 154 (2006) 8–17.

38 D. Natarajan, T.V. Nguyen, J. Electrochem. Soc. 148 (2001) A1324–A1335.

39 J.H. Jang, W.M. Yan, C.C. Shih, J. Power Sources 161 (2006) 323–332.

40 Z. Liu, Z. Mao, C. Wang, J. Power Sources 158 (2006) 1229–1239.

41 H.S. Chu, C. Yeh , F. Chen, J. Power Sources. 123 (2003) 1–9.

42 J.T. Gostick, M.A. Ioannidis, M.W. Fowler, M.D. Pritzker, J. Power Sources 173 (2007) 277–290.

43 J.G. Pharoah, J. Power Sources 144 (2005) 77–82.

44 A.S. Rawool, S.K. Mitra, J.G. Pharoah, J. Power Sources 162 (2006) 985–991.

45 X.D. Niu, T. Munekata, S.A. Hyodoa, K. Suga, J. Power Sources 172 (2007) 542–552.

46 J.H. Nam, M. Kaviany, Int. J. Heat Mass Transfer 46 (2003) 4595–4611.

47 U. Pasaogullari, C.Y. Wang, Electrochim. Acta 49 (2004) 4359–4369.

48 U. Pasaogullari, C.Y. Wang, J. Electrochem. Soc. 151 (2004) A399–A406.

49 X. Zhu, P.C. Sui, N. Djilali, J. Power Sources 172 (2007) 287–295.

50 P.C. Sui, N. Djilali, J. Power Source 161 (2006) 294–300.

51 V.P. Schulz, J. Becker, A. Wiegmann, P.P. Mukherjee, C.Y Wang, J. Electrochem. Soc. 154 (2007) B419–B426.

52 L. Zhang, Y. Liu, H. Song, S. Wang, Y. Zhou, S.J. Hu, J. Power Sources 162 (2006) 1165–1171.

53 P. Zhou, C.W. Wu, G.J. Ma, J. Power Sources 159 (2006) 1115–1122.

54 P. Zhou, C.W. Wu, J. Power Sources 170 (2007) 93–100.

55 P. Zhou, C.W. Wu, G.J. Ma, J. Power Sources 163 (2007) 874–881.

56 W. Sun, B.A. Peppley, K. Karan, J. Power Sources 144 (2005) 42–53.

57 I. Nitta, T. Hottinen, O. Himanen, M. Mikkola, J. Power Sources 171 (2007) 26–36.

58 I. Nitta, O. Himanen, M. Mikkola, Thermal conductivity and contact resistance of compressed gas diffusion layer of PEM fuel cell, Fuel Cells, submitted for publication.

59 I. Nitta, O. Himanen, M. Mikkola, Contact resistance between gas diffusion layer and catalyst layer of PEM fuel cell, Electrochem. Commun. In press.

60 T. Hottinen, O. Himanen, S. Karvonen, I. Nitta, J. Power Sources 171 (2007) 113–121.

61 D.M. Bernardi, M.W. Verbrugge, J. Electrochem. Soc. 139 (1992) 2477–2491.

62 O. Himanen, T. Hottinen, M. Mikkola, V. Saarinen, Electrochim. Acta 52 (2006) 206–214.

63 Manufacture's data sheet for ISEM-3 graphite by Svenska Tanso AB.

64 S. Cleghorn, J. Kolde, W. Liu, in:W. Vielstich, A. Lamm, H. Gasteiger (Eds.), Handbook of Fuel Cells, John Wiley & Sons, Ltd., New York, 2003, pp. 566–575.

65 Manufacturer's Data Sheet for ®Sigracet GDL 10 BA by SGL Carbon AG.

66 W. Sun, B.A. Peppley, K. Karan, Electrochim. Acta 50 (2005) 3359–3374.

67 D. Natarajan, T.V. Nguyen, J. Power Sources 115 (2003) 66–80.

68 T. Hottinen, O. Himanen, Electrochem. Commun. 9 (2007) 1047–1052.

69 W.Q. Tao, C.H. Min, X.L. Liu, Y.L. He, B.H. Yin, W. Jiang, J. Power Sources 160 (2006) 359–373.

70 C.H. Min, Y.L. He, X.L. Liu, B.H. Yin, W. Jiang, W.Q. Tao, J. Power Sources 160 (2006) 374–385.

71 H. Ju, C.Y.Wang, J. Electrochem. Soc. 151 (2004) A1954–A1960.

ISBN 978-951-22-9218-9 (PDF)
ISSN 1459-7268 (PDF)